Case Studies in Nondestructive Testing and Evaluation ••• (••••) •••–•••

Contents lists available at ScienceDirect

Case Studies in Nondestructive Testing and Evaluation

www.elsevier.com/locate/csndt

Dual energy CT inspection of a carbon fibre reinforced plastic composite combined with metal components

Daniel Vavrik [a,b,*], Jan Jakubek [b], Ivana Kumpova [a], Martin Pichotka [b]

[a] Institute of Theoretical and Applied Mechanics, v.v.i., Centre of Excellence Telč, Czech Republic
[b] Institute of Experimental and Applied Physics, Czech Technical University in Prague, Czech Republic

ARTICLE INFO

Article history:
Available online xxxx

ABSTRACT

This work is focused on the inspection of carbon fibre reinforced plastic composites (CFRP) combined with metal components. It is well known that the high absorption of metallic parts degrades the quality of radiographic measurements (contrast) and causes typical metal artefacts in X-ray computed tomography (CT) reconstruction. It will be shown that these problems can be successfully solved utilizing the dual energy CT method (DECT), which is typically used for the material decomposition of complex objects. In other words, DECT can help differentiate object components with a similar overall attenuation or visualise low attenuation components that are next to high attenuation ones. The application of DECT to analyse honeycomb sandwich panels and CFRP parts joined with metal fasteners will be presented in the article.

1. Introduction

The inspection of sandwich structures composed of a metallic honeycomb core and a CFRP skin, widely used in the aerospace industry, will be presented in this work as the first show case. In particular, the combination of a CFRP skin and an aluminium (Al) core is investigated due its superior strength-to-weight ratio and excellent impact resistance. Possible skin-to-core disbonds may have a crucial influence on the structural integrity of such structures. However, their identification can be problematic when utilizing standard non-destructive techniques (NDT) like ultrasound, thermography, or tap testing methods due to their relatively low resolution and the intrinsically high heterogeneity of honeycomb sandwich structures. The standard X-ray computed tomography (X-ray CT) technique provides good results if the inspected object is flat and tilted in the optimal position to identify disbonds searching the reconstructed volume slice by slice. Direct 3D visualisation is rather problematic, especially if the object is not flat. It will be shown here that this restriction can be successfully overcome utilizing the dual energy computed tomography method (DECT). Furthermore, the identification of disbonding can be achieved by employing a single photon counting detector with a spectroscopic capability, allowing multi-energy CT. The porosity of CFRP skin is obviously another parameter which has to be analysed. It will be shown that a porosity analysis based on X-ray CT data can be significantly influenced by the porosity present in the resin layer bonding skin and the core of the sandwich structure. Yet again, this problem can be solved utilizing the DECT method.

The identification of disbonding present between CFRP components, with a copper (Cu) grid on the top, glued together and joined with metal fasteners, will be shown here as another show case. The identification of disbonding due to a lack of resin is complicated by metal artefacts as well as by the beam hardening effect caused by the significantly differing

* Corresponding author.
E-mail addresses: vavrik@itam.cas.cz (D. Vavrik), jan@jakubek.cz (J. Jakubek), kumpova@itam.cas.cz (I. Kumpova), pichotka@utef.cvut.cz (M. Pichotka).

http://dx.doi.org/10.1016/j.csndt.2016.05.001
2214-6571/

Please cite this article in press as: Vavrik D, et al. Dual energy CT inspection of a carbon fibre reinforced plastic composite combined with metal components. Case Stud Nondestruct Test Eval (2016), http://dx.doi.org/10.1016/j.csndt.2016.05.001

attenuation of the specimen components (CFRP, Cu mesh, steel). It was proven that it is almost impossible to identify disbonded areas utilizing standard tomography techniques; however, disbonded areas can be clearly identified utilizing DECT tools.

2. Dual energy computed tomography

2.1. Material decomposition

The basic idea of DECT has been known quite for a while [1,2]; it is based on the fact that material components presented in a complex object can be distinguished utilizing two low energy (LE) and high energy (HE) CT, measured with different X-ray spectra. Related material decomposition is based on the fact that differences between the attenuation coefficients of materials with different atomic number significantly increase with decreasing tube potential, while at high energies (>∼100 keV) this change is much slower. Such material decomposition can be done in a pre-reconstruction space (projection) or a post-reconstruction (image) space. The advantage of a post-reconstruction analysis lies in its relatively easy implementation; therefore, it was employed in this work.

The image displayed in computed tomography is composed of a matrix of scaled linear attenuation coefficients [2]. As such, the attenuation coefficients are energy dependent, and the observed values are related to the spectrum of energies present in the X-ray beam. On other hand, it has been shown that the reconstructed values correspond to a particular effective energy [3]. The concept of effective energy (and the effective linear attenuation coefficient) is valid within the entirety of an inspected object, if the beam hardening effect can be neglected (small or low Z object) or if this effect is appropriately corrected.

An appropriate beam hardening correction of radiograms (CT projections) can be done utilizing the Signal to equivalent thickness method [4]. The calibration is performed with a set of flat and homogeneous absorbers, ideally with the identical material composition as the inspected object. The dependence of the detected count rate on the absorber thickness is measured, and the calibration function is calculated for each detector pixel. This function translates the intensity images into the equivalent thickness, and CT projections are linearized in this way. Although it is not possible to manufacture calibration absorbers from the same material as the inspected object in many cases, calibration functions can be shaped into the right form if the object thickness is known [5]. Moreover, monochromatised data can be obtained if the calibrated data are transformed back into intensities; therefore, the concept of effective energy can be utilized for the calibrated data if the object is made from a single material. Nevertheless, reasonable results are obtained for composite objects if the calibration is done with respect to the prevalent material presented in the object.

Since different materials have deviating X-ray attenuation at different X-ray energies, we can calculate the composition of a given voxel of the reconstructed volume. The effective linear attenuation coefficient in each volume element of a CT image can be expressed as a linear combination of the attenuation coefficients of the basis materials multiplied by their volume fraction [6].

$$\mu_{\mathrm{LE}} = f_1\mu_{1\mathrm{LE}} + f_2\mu_{2\mathrm{LE}} \tag{1}$$

$$\mu_{\mathrm{HE}} = f_1\mu_{1\mathrm{HE}} + f_2\mu_{2\mathrm{HE}} \tag{2}$$

Where f_1, f_1 are the fractions made up by the first and second materials, respectively, μ_{LE} and μ_{HE} are the effective linear attenuation coefficients of the mixture at low and high energies, and $\mu_{1\mathrm{LE}}$ and $\mu_{2\mathrm{HE}}$ are attenuation coefficients of the constituents at low and high energies. Fractions of the constituents derived from equation (1) can be expressed as follows:

$$f_1\left(\mu_{1\mathrm{HE}} - \mu_{1\mathrm{LE}}\frac{\mu_{2\mathrm{HE}}}{\mu_{2\mathrm{LE}}}\right) = \mu_{\mathrm{HE}} - \frac{\mu_{2\mathrm{HE}}}{\mu_{2\mathrm{LE}}}\mu_{\mathrm{LE}} \tag{3}$$

$$f_2\left(\mu_{2\mathrm{HE}} - \mu_{2\mathrm{LE}}\frac{\mu_{1\mathrm{HE}}}{\mu_{1\mathrm{LE}}}\right) = \mu_{\mathrm{HE}} - \frac{\mu_{1\mathrm{HE}}}{\mu_{1\mathrm{LE}}}\mu_{\mathrm{LE}} \tag{4}$$

Let's suppose: LE and HE are significantly different (these being the basic conditions for successful material decomposition); the first material component has a lower atomic number than the second one. In this case the expression in the brackets (4) has a negative value, so equation (4) can be changed as follows to have a positive left side part of this equation:

$$f_2\left(\mu_{2\mathrm{LE}} - \mu_{2\mathrm{HE}}\frac{\mu_{1\mathrm{LE}}}{\mu_{1\mathrm{HE}}}\right) = \mu_{\mathrm{LE}} - \frac{\mu_{1\mathrm{LE}}}{\mu_{1\mathrm{HE}}}\mu_{\mathrm{HE}} \tag{5}$$

The expressions in the brackets (3), (5) are a material constant for a given X-ray spectrum. The linear attenuation coefficients for the two basis materials μ_1 and μ_2 at low and high energies can be calibrated from the CT images containing the respective materials. In practice, CT numbers (hereafter, the abbreviation C will be used) are often used as they are the scaled version of the effective linear attenuation coefficients. The CT numbers in this work are not equivalent to Hounsfield units, but simply represent the attenuation values obtained from tomographic reconstruction. Consequently, we can rewrite equations (3) and (5) into the forms:

Please cite this article in press as: Vavrik D, et al. Dual energy CT inspection of a carbon fibre reinforced plastic composite combined with metal components. Case Stud Nondestruct Test Eval (2016), http://dx.doi.org/10.1016/j.csndt.2016.05.001

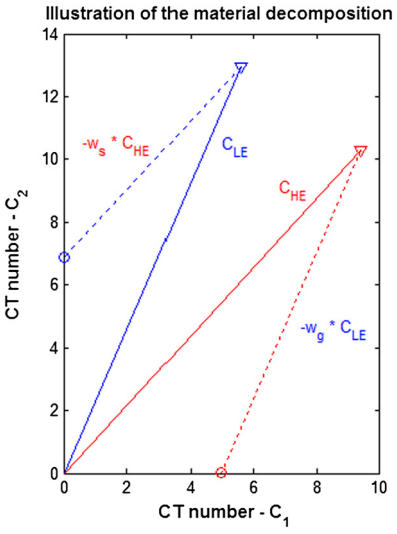

Fig. 1. Illustration of the algorithm. The CT numbers from the low and high energy measurements can be seen as vectors with different CT numbers of the first and second constituents [C_1, C_2]. The linear operator w is used to cancel out the related constituent from the reconstructed volume.

$$F_1 = C_{\mathrm{HE}} - w_2 C_{\mathrm{LE}} \tag{6}$$

$$F_2 = C_{\mathrm{LE}} - w_1 C_{\mathrm{HE}} \tag{7}$$

Where F_1 and F_2 have the meaning of the scaled fraction of constituents 1 and 2, respectively. Weighting factors w_1, w_2 can be calculated utilizing local CT numbers C^l, taken from the reconstructed volume in places where only one constituent is presented:

$$w_1 = C^l_{1\mathrm{HE}}/C^l_{1\mathrm{LE}} \quad \text{and} \quad w_2 = C^l_{2\mathrm{LE}}/C^l_{2\mathrm{HE}} \tag{8}$$

The weighting factors can also be found heuristically if it is not to use the calculations above for some reason (e.g. material compounds, more than three constituents, significant beam hardening effect etc.). The material decomposition algorithm based on equations (6) and (7) is illustrated in Fig. 1. The CT numbers from the low and high energy measurements C_{LE} and C_{HE} can be seen as vectors with different CT numbers of the first and second materials: $C_{\mathrm{LE}} = [C_{1\mathrm{LE}}, C_{2\mathrm{LE}}]$ and $C_{\mathrm{HE}} = [C_{1\mathrm{HE}}, C_{2\mathrm{HE}}]$. The angle between these vectors is dependent on the difference between the attenuation coefficients of the constituents and on the differentiation of the LE and HE spectra. It is clear that the angle should be as large as possible to avoid an undesirable reduction of the SNR. Correct choice of LE and HE spectra is a highly demanding problem which has no trivial solution for an unknown measurement. However, obviously in general, well-separated X-ray spectra provide better results than strongly overlapping X-ray spectra [7]. This is achieved by the appropriate choice of the acceleration voltage and X-ray beam pre-filtering (detector energy threshold) considering detector efficiency and specimen attenuation. In case of spectroscopic detectors the choice of different thresholds allows for decomposition from a single measurement.

2.2. Instrumentation

The DECT instrumentation from the point of view of LE and HE energies can generally be based on two principles: utilizing two differing X-ray spectra (no special requirements for the detector) or splitting of the X-ray spectra into two (or more) bands utilizing energy thresholds which are set on the detector side (presuming that the detector has this capability). X-ray tube spectra can be influenced by the tube voltage and/or X-ray beam filtering.

The DECT measurement can be performed twice as fast using a dual source CT (DSCT) setup, where two independent imaging lines are installed. Without the technology to employ two energies at once in a single scan, the object has to be scanned twice, i.e. leading to doubling the scanning time. The first medical DECT/DSCT scanner [8] brought fast scanning of the living body with the possibility to resolve soft tissues from bones. However, the spatial resolution of this scanner is limited by fixed irradiation geometry, as is the case for most medical scanners.

The dual source/dual energy CT scanner developed in-house [9–11] installed in the Centre of Excellence Telč (CET), Czech Republic, allows for the inspection of objects using variable magnification (resolution) in adjustable acceleration voltages, see Fig. 2. The additional shaping of X-ray spectra is achieved by appropriate filtering. This DECT scanner is equipped with two large area flat panel detectors, a positioning system comprising 14 axes, and a precise air bearing rotational stage. A large area single photon counting detector [12] allowing for energy thresholding can also be utilized as an alternative approach for dual (multi) energy measurements. This detector has proven to be advantageous, especially for low attenuation objects.

Please cite this article in press as: Vavrik D, et al. Dual energy CT inspection of a carbon fibre reinforced plastic composite combined with metal components. Case Stud Nondestruct Test Eval (2016), http://dx.doi.org/10.1016/j.csndt.2016.05.001

X-ray Tubes:
XWT160, spot size 1 μm @ 9W, 5 μm @ 20W
XWT240, spot size 5 μm @ 20 W
X-ray Detectors:
2 × Flat Panel Detector Perkin Elmer
2048 × 2048 px, 200 μm pixel pitch
Single photon counting detector
2560 × 2560 px, 55 μm pixel pitch
Rotational Stages:
Aerotech APR150, 1.5 μm accuracy
Aerotech ABRT 50, 150 nm accuracy
2 revolvers with filters for beam hardening corrections and for beam filtering.

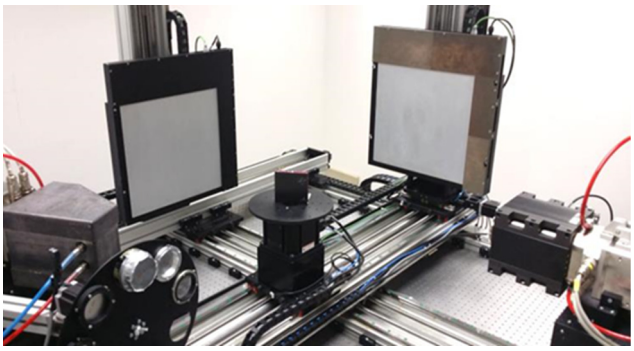

Fig. 2. Dual source/dual energy X-ray μ-CT scanner.

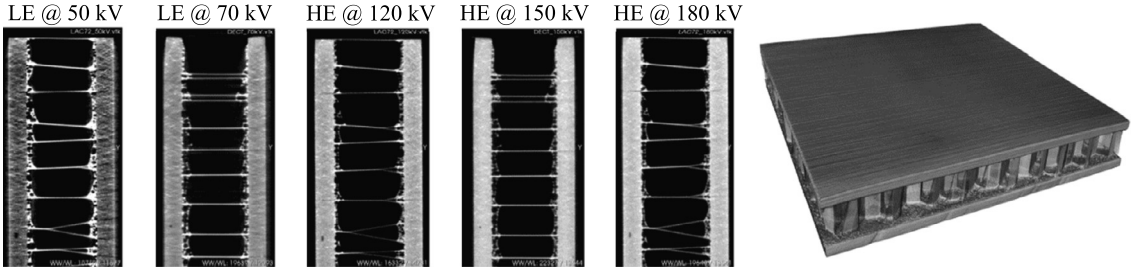

Fig. 3. Influence of the tube spectra on a reconstruction – beam hardening artefacts increase as tube potential decreases. The glue layer is most pronounced at the lowest potential, as scattering artefacts increase as potential increases. For illustrative purposes, the 3D visualisation of the reconstructed volume is depicted (right).

3. Inspection of a honeycomb panel with a metal core and CFRP skin

The inspected honeycomb sandwich has two basic components – CFRP skins (each made from 10 layers of unidirectional prepreg EH 420C) and an Al honeycomb core (10 mm thick, foil thickness 0,15 mm, cell size 6 mm), which are glued together (AF163-2K-wt0.06). The total thickness of the sandwich is 15 mm. An artificially disbonded region (lack of glue) between the skin and the core was prepared on one side of the sample.

To find the right DECT parameters, CT measurements were done at five X-ray tube potentials utilizing a Perkin Elmer detector: 50 and 70 kV for LE, 120, 150, and 180 kV for HE. The X-ray spectra were shaped by a 1.5 mm thick Al filter for LE potentials and a 1.4 mm thick Cu filter for HE potentials. A beam hardening correction [4] was applied for all the CT projection data acquired. The reconstructed volumes have a 65 μm voxel size due to irradiation geometry and detector pixel size. Consequently, only relatively large pores can be identified. The influence of the tube potential on the tomographic reconstruction is documented in Fig. 3. Finally, the 70 kV tube potential was chosen for the LE data – beam hardening artefacts were much more pronounced for the lower potential; the 150 kV tube potential was selected for the HE data – scattering artefacts and contrast were worse for the higher tube potential.

3.1. Evaluation of porosity

Porosity in the CFRP material is one of parameters which is standardly inspected. So far, it has been shown that the evaluation of a honeycomb skin porosity can be misinterpreted due to porosity within the glue layer – pores presented in the skin and not in the glue layer are important from the point of view of structure reliability. Therefore, glue suppression in the reconstructed volume utilizing the DECT approach is helpful for the skin porosity calculation. It was found that the skin (constituent 1) has a lower attenuation than the glue layer (constituent 2). The weight factor w_2 for the DECT equation (6) was calculated (8), utilizing LE and HE reconstructed data: $w_2 = C^l_{2\mathrm{LE}}/C^l_{2\mathrm{HE}}$. More specifically, local CT numbers $C_{2\mathrm{LE}}$ and $C_{2\mathrm{HE}}$ were calculated from the region containing glue layer only. As a result of this evaluation, we apply:

$$F_{\mathrm{skin}} = C_{150\,\mathrm{kV}} - 0.76C_{70\,\mathrm{kV}} \tag{9}$$

The related procedure is visualized in Fig. 4, where the DECT volume with suppressed glue layer and honeycomb was obtained. Note that the glue layer and honeycomb walls are much more pronounced for the LE tube potential when compared to the HE tube potential. The honeycomb walls are actually thinner than voxel size; therefore, the related CT numbers are much lower than they would be at a higher CT resolution.

The influence of the reconstructed data type on the porosity calculation is documented in Fig. 5. Many small pores were identified in the glue layer for both LE and HE potentials near the skin surface, while these pores completely disappeared in the DECT volume. Note that porosity calculated for LE data is more than twice as large as for DECT.

Please cite this article in press as: Vavrik D, et al. Dual energy CT inspection of a carbon fibre reinforced plastic composite combined with metal components. Case Stud Nondestruct Test Eval (2016), http://dx.doi.org/10.1016/j.csndt.2016.05.001

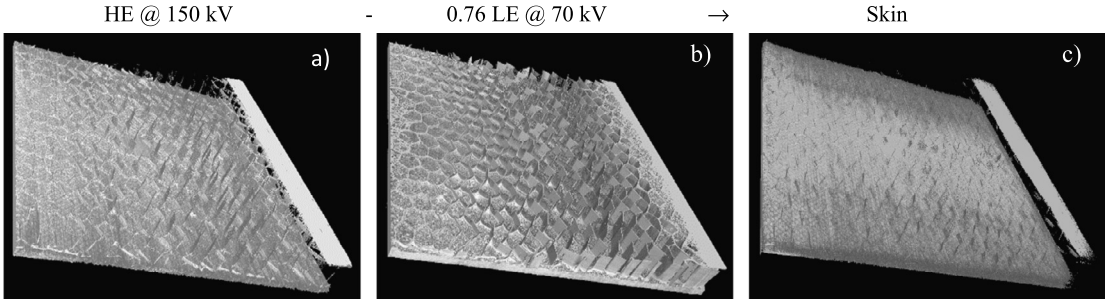

Fig. 4. Separation of the skin, utilizing DECT tools: a) reconstruction for HE data; b) the honeycomb and glue layers are most pronounced for the low tube potential; these components are significantly suppressed for the DECT reconstruction (c).

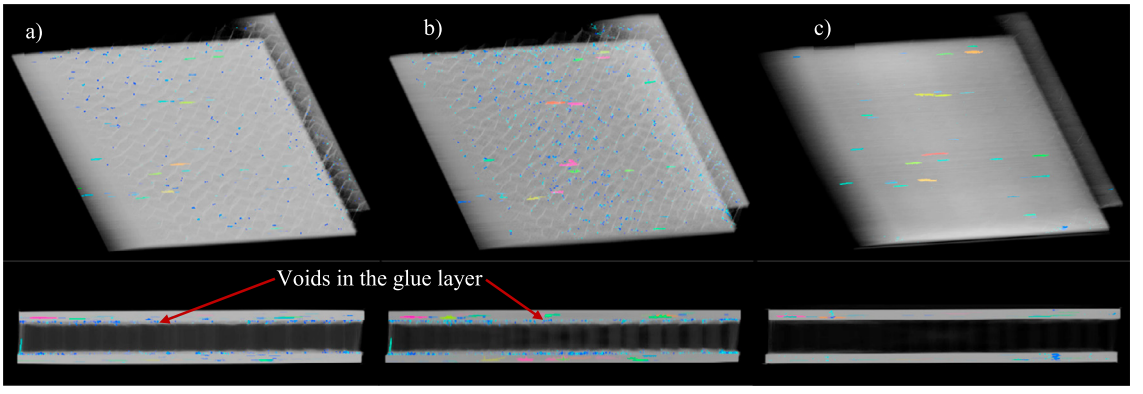

Fig. 5. Influence of the DECT subtraction on the porosity calculation. Total porosity calculated: a) 0.07 % for data taken at a 150 kV tube potential; b) 0.12 % for data taken at 70 kV, c) 0.05 % for DECT data. It is clearly visible from the bottom images (side view of the reconstructed volume) that this discrepancy mostly arises from the pores identified in the glue layer near the skin boundary (these pores are not relevant from point of view of structure reliability). Most of voids in the skin have a needle shape with a relatively large volume.

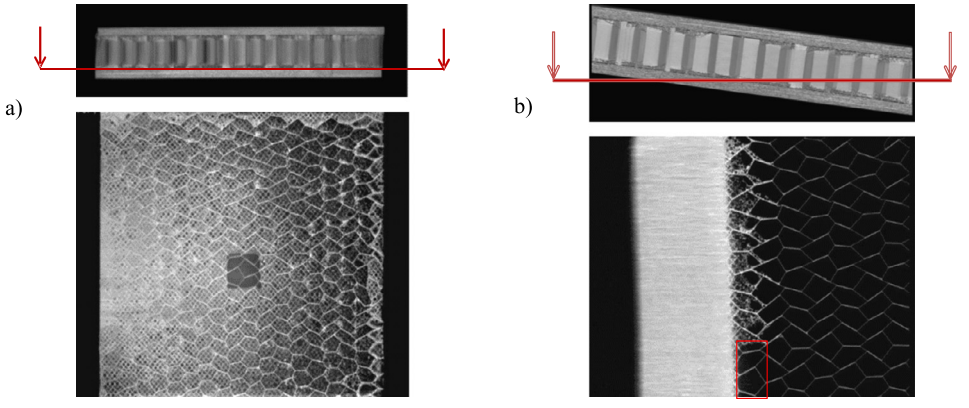

Fig. 6. Identification of the disbonded area in a simple CT reconstruction. The whole area is clearly visible when a specific tomographic slice of the object is correctly oriented (a). The same disbonding is only partially visible in the slice if this same object is observed at an angle (b).

3.2. Identification of disbonding

Identification of the disbonded area is straightforward if the specimen is flat and if CT reconstruction of the object is oriented along one main axis of the volume; see Fig. 6a). However, if the orientation is not optimal, the identification of such defects is rather hard; see Fig. 6b). For an object of complex shape, simple visual defect identification from the 3D visualisation is therefore hardly a viable solution.

The problem that the disbonded region is hard to distinguish directly from a 3D visualisation proved to be true for every X-ray tube potential and energy threshold applied. Among other reasons, the glue layer cannot be separated using thresholding due to the beam hardening effect and scattering (signal from the core and glue is strongly propagated into the skin). The 3D visualisation of the disbonding for LE at 70 kV is depicted in Fig. 7a). The disbonded region slightly differs

Please cite this article in press as: Vavrik D, et al. Dual energy CT inspection of a carbon fibre reinforced plastic composite combined with metal components. Case Stud Nondestruct Test Eval (2016), http://dx.doi.org/10.1016/j.csndt.2016.05.001

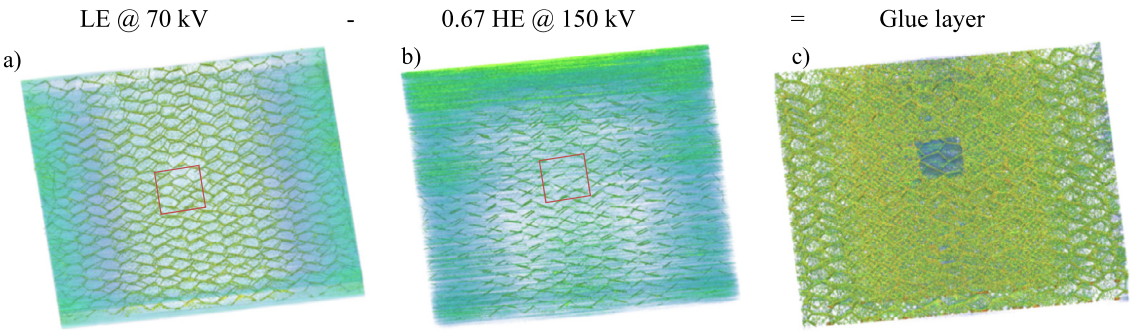

Fig. 7. Disbonded area is almost invisible in a 3D representation of the CT data at LE a) and HE b); however, it is clearly visible in the DECT image c).

(marked by the region outlined in red), but it is not clearly visible. Disbonding is practically invisible (marked by the region outlined in red) for CT data taken at 150 kV; see Fig. 7b).

It was found that visualisation of the disbonded area can be significantly enhanced utilizing DECT material decomposition. The weight factor w_1 for the DECT equation (7) was calculated (8), utilizing LE and HE reconstructed data: $w_1 = C^l_{1\mathrm{HE}}/C^l_{1\mathrm{LE}}$. Local CT numbers $C_{1\mathrm{LE}}$ and $C_{1\mathrm{HE}}$ were calculated as median of the region containing skin only. As a result of this evaluation, we apply:

$$F_{\mathrm{glue}} = C_{70\,\mathrm{kV}} - 0.67 C_{150\,\mathrm{kV}} \tag{10}$$

The resulting image is depicted in Fig. 7c), for which disbonding is directly visible in 3D, since the skins were significantly suppressed in the DECT reconstructed volume. This clear visualisation occurs, because the glue layer is separated as an individual material within the reconstructed volume.

3.3. Identification of disbonding based on spectroscopic data

Analogous to the previous approach, we seek to identify the disbonded area of the sample utilizing a large area single photon counting detector [12]. A Hamamatsu L10101 X-ray tube, featuring a Tungsten target, operated at 90 kV and equipped with a 0.4 mm Al filter was employed in the measurements. The lower threshold of the single photon counting detector was set to 10 keV and 18 keV, respectively, cutting off photons below this threshold. Both energy channels were reconstructed using an in-house total variation maximum likelihood constrained based iterative reconstruction routine [13]. This allows a high-quality reconstruction at a significantly reduced number of projections compared to standard FBP, 360 projections in this case. The reconstruction routine features an alternating-direction based sparsity-inducing method; successive subsets of OSEM here are alternated with the steepest gradient routine minimizing the L1 norm of the reconstructed volume. The step-size of the L1 minimization is dynamically adapted to the step-size of the OSEM routine; a Kalman-type filter is applied to the timeline of each voxel to dampen the oscillations of density values.

To isolate the glue layer, spectroscopic data are taken into account. The deviating spectroscopic behaviour of the different constituents of the sample is exploited to this end. Using the appropriate energy bins, we are able to isolate a certain material within the volume by taking the difference-image of the two measured energy-spectra. Due to the low statistics of the difference image, this channel was subsequently weighted by the sum of the 10 keV and 18 keV channels. Also, a gradient-descent TV-min algorithm was used to smooth the resulting image. For an overlaying of the gray-scaled rendering of the volume by this channel, see Fig. 8. It can be observed that we clearly isolated the glue within the volume [14].

4. Inspection of CFRP components glued together and joined with a metal fastener

The inspected sample has three basic material components: CFRP (two 1.2 mm thick flat parts, each from 6 layers), a metal fastener (steel rivet Avinox II), and a Cu grid (for conductivity improvement, type 4AE420539) on the top of each CFRP plate. Artificial disbonding between the glued CFRP parts was prepared in the rivet's vicinity. For a schematic drawing and a photograph of the sample see Fig. 9.

As mentioned in the previous section, the LE and HE X-ray spectra have to be separated as much as possible. However, the LE potential should be as low as possible for this reason, but high enough to be able penetrate all parts of inspected sample (especially the steel rivet) with satisfactory efficiency.

The CT measurement was done using a Perkin Elmer detector: LE at 80 kV with an Al alloy filter and HE at 160 kV with a tin filter, respectively. The tomographic measurements were done with the following parameters: voxel size for all reconstructions was 20 µm, CT data was taken at 1200 projections, 3×1 sec exposure for each one. Data reconstructions were done utilizing the Volex 6 software. The 3D visualisations (VGstudio Max) of the CT reconstruction of the LE and HE data are depicted in Fig. 10. It is clearly visible that the beam hardening effects as well as metal artefacts are strongly pronounced in both cases. The disbonded area marked by the yellow line is hard to resolve.

Please cite this article in press as: Vavrik D, et al. Dual energy CT inspection of a carbon fibre reinforced plastic composite combined with metal components. Case Stud Nondestruct Test Eval (2016), http://dx.doi.org/10.1016/j.csndt.2016.05.001

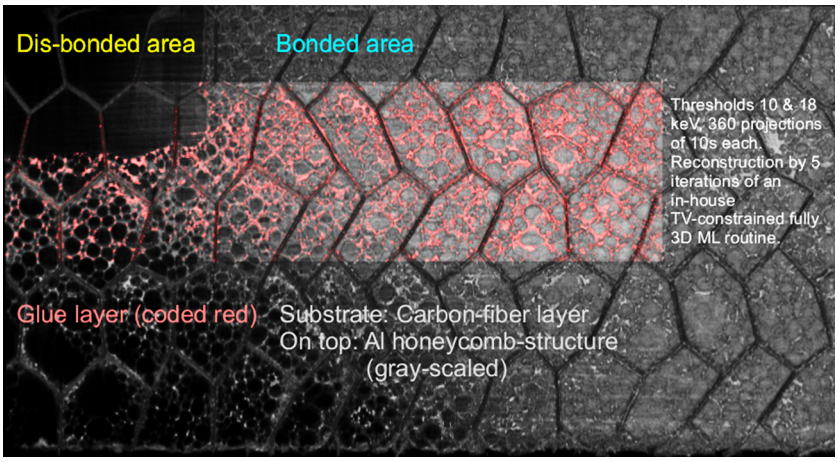

Fig. 8. Gray-scaled rendering of the reconstructed volume. Within the rectangular area, the rendered volume was overlaid by the material-decomposed data (coded in red). The glue is clearly isolated from the other constituents of the volume.

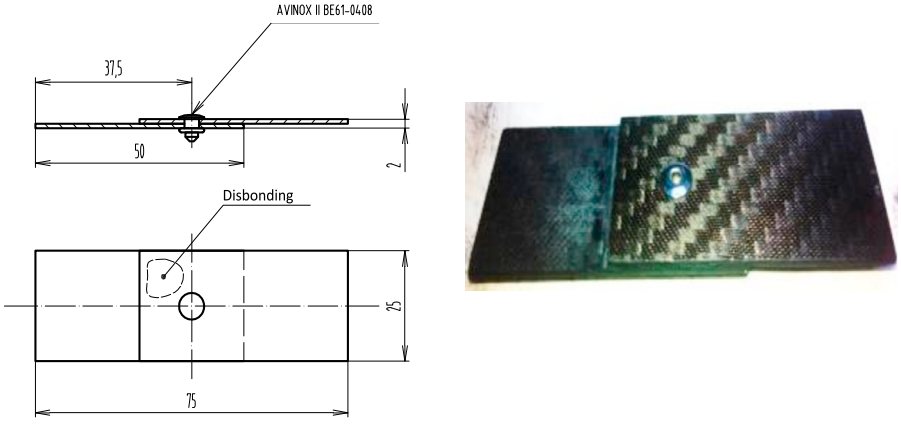

Fig. 9. Schematic drawing of the inspected sample (left), photograph (right).

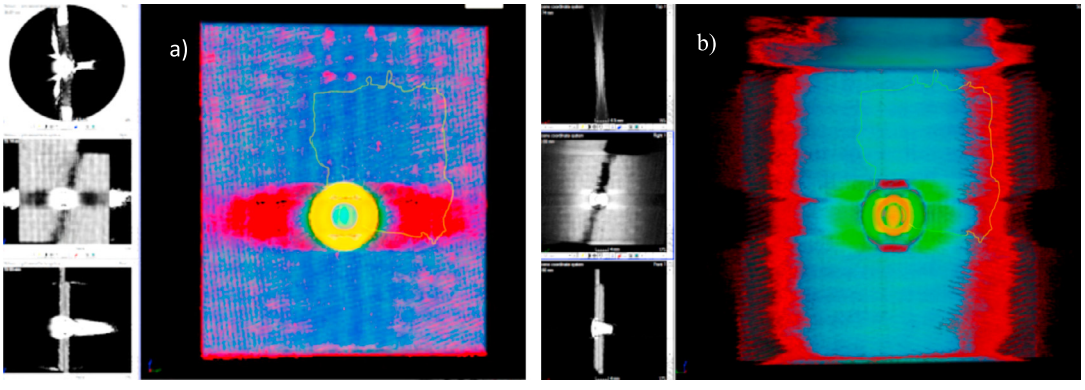

Fig. 10. Visualisation of the CT reconstruction: a) – data taken at LE, almost no evidence of disbonding (its expected area is marked by the yellow line); b) – data taken at HE at 160 kV, disbonded area is slightly visible, but the beam hardening effect caused by the Cu mesh is strongly pronounced.

It will be shown that identification of the disbonded area can be efficiently performed by DECT tools. Analogous to the previous section, image-based DECT was utilized using the weighted subtraction equation (6). Contrary to the previous section, the weighting factor calculation was based on the signal profile passing the CFRP, influenced by the metal artefact effect.

A CT reconstruction of a single slice based on LE data is imaged in Fig. 11 (left) and the same slice based on HE data (right), respectively. Note that the CFRP structure is better visible for LE data, but the metal artefacts are more pronounced.

Please cite this article in press as: Vavrik D, et al. Dual energy CT inspection of a carbon fibre reinforced plastic composite combined with metal components. Case Stud Nondestruct Test Eval (2016), http://dx.doi.org/10.1016/j.csndt.2016.05.001

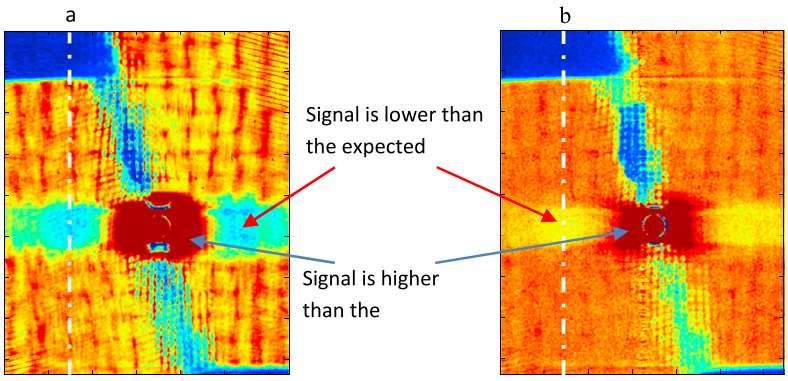

Fig. 11. CT reconstruction based on LE @ 80 kV data (left), CT reconstruction based on HE @ 160 kV (right).

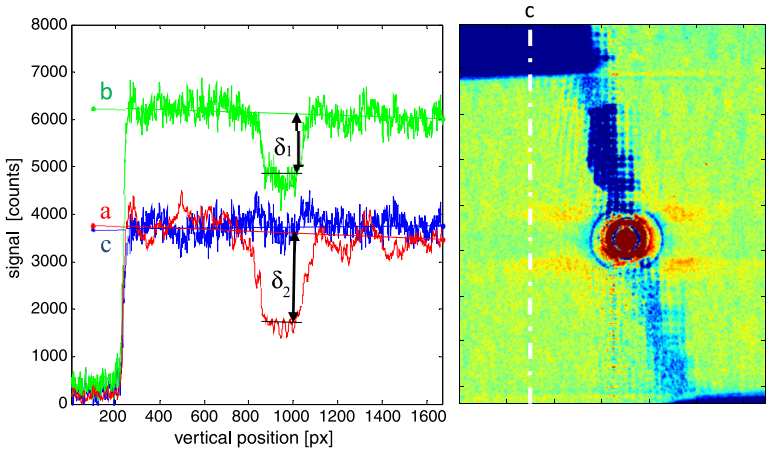

Fig. 12. Signal profiles are marked by the white dashed lines at left. The DECT slice is at right.

The density appears to be higher around the steel rivet in both reconstructions. Some vertical lines, in the graph they are labelled by *a* and *b*, pass through areas where the density is significantly lower than expected due to metal artefacts.

The corresponding signal profiles are plotted in Fig. 12 (left) – drop downs corresponding to the areas indicate lower apparent density. The relative amplitude of these profiles depends on w_2 as follows:

$$w_2 = -\delta_2/\delta_1 \tag{11}$$

The resulting weighting factor used in our analysis is $w_2 = 0.62$. Consequently, equation (6) reads here:

$$F = C_{160\,\mathrm{kV}} - 0.62 C_{80\,\mathrm{kV}} \tag{12}$$

The resulting DECT slice obtained from equation (1) is depicted in Fig. 12 (right). Note that both metal artefact effects – lowered, as well as increased density, are clearly suppressed. The related density profile *c* is plotted in blue in Fig. 12 (left).

Visualisation of the result based on DECT is shown in Fig. 13. These results demonstrate that a disbonded area is very clearly visible in 3D just by utilizing basic data thresholding (compare with Fig. 10). Also, the metal artefacts throughout the volume have been successfully suppressed here with the exception of some area close to the actual rivet, as may be caused by some small angle scattering. A rendering of the entire reconstructed volume is displayed (right).

5. Conclusions

In this paper, it was shown that dual energy CT is capable of reducing reconstruction artefacts within composite materials of strongly heterogeneous absorption behaviour.

Also, spectroscopic tomography and DECT strongly simplify identification of disbonded areas in volumetric data.

Furthermore, isolation of the glue layer allows for correctly determining the porosity of the CFRP layer without any contributions from the glue layer. In the sample analysed in this paper, this contribution results a reducting by a factor two of the total porosity.

Please cite this article in press as: Vavrik D, et al. Dual energy CT inspection of a carbon fibre reinforced plastic composite combined with metal components. Case Stud Nondestruct Test Eval (2016), http://dx.doi.org/10.1016/j.csndt.2016.05.001

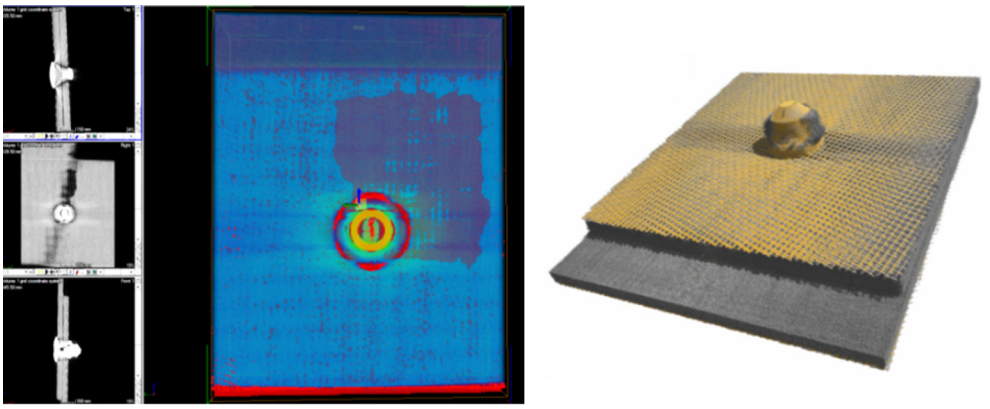

Fig. 13. Visualisation of the image based on DECT data (left), the disbonded area is clearly visible, and the metal artefacts have disappeared. The whole reconstructed specimen is imaged (right) for illustrative purposes.

It was also shown that disbonding due to a lack of resin between CFRP parts joined with a metal fastener is hard to resolve when employing standard tomography due to the strong metal artefacts and the beam hardening effect. However, this disbonded area can be clearly identified in the DECT data.

In general, the presented DECT techniques can be applied to any complex structures where material decomposition is advantageous to allow the constituents to be analysed separately.

Acknowledgements

This work was supported by the QUICOM project funded by the 7th EU Framework Programme under Grant Agreement No. ACP2-GA-2012-314562, partially also supported by Project No. LO1219 under the Ministry of Education, Youth and Sports and GA15-07210S of the Czech Science Foundation. The data were reconstructed using the Volex 6 software provided by the Fraunhofer Development Center X-ray Technology EZRT in Furth, Germany. The tomographic visualisations were done utilizing Volume Graphic GmbH software VGStudio MAX.

References

[1] Alvarez RE, Macovski A. Energy-selective reconstructions in X-ray computerized tomography. Phys Med Biol 1976;21:733–44.
[2] Millner MR, McDavid WD, Waggener RG, Dennis MJ, Payne WH, Sank VJ. Extraction of information from CT scans at different energies. Med Phys 1979;6:70–1. http://dx.doi.org/10.1118/1.594555.
[3] McCullough EC, Baker HL Jr., Houser OW, Reese DF. An evaluation of the quantitative and radiation features of a scanning X-ray transverse axial tomography: the EMI scanner. Radiology 1974;111.
[4] Jakubek J. Data processing and image reconstruction methods for pixel detectors. Nucl Instrum Methods A 2007;576:223–34. http://dx.doi.org/10.1016/j.nima.2007.01.157.
[5] Vavrik D. CT artefact reduction by signal to thickness calibration function shaping. Nucl Instrum Methods A 2011;633:152–5.
[6] Vinegar HJ, Wellington SL. Tomographic imaging of three phase flow experiments. Rev Sci Instrum 1987;58:96–107.
[7] Johnson TR. Dual-energy CT: general principles. Am J Roentgenol 2012;199:S3–8. http://dx.doi.org/10.2214/AJR.12.9116.
[8] Johnson TR, Nikolaou K, Wintersperger BJ, et al. Dual-source CT cardiac imaging: initial experience. Eur Radiol 2006;16:1409–15.
[9] Patent EP2835631 – a multi-axial apparatus for carrying out X-ray measurements, particularly computed tomography.
[10] Fíla T, Kumpova I, Jandejsek I, Kloiber M, Turecek D, Vavrik D. Utilization of dual-source X-ray tomography for reduction of scanning time of wooden samples. J Instrum, JINST 2015;10:C05008. http://dx.doi.org/10.1088/1748-0221/10/05/C05008.
[11] Fila T, Kumpova I, Koudelka P, Zlamal P, Vavrik D, Jirousek O, et al. Dual-energy X-ray micro-CT imaging of hybrid Ni/Al open-cell foam. J Instrum, JINST 2016:C01005. http://dx.doi.org/10.1088/1748-0221/11/01/C01005.
[12] Jakubek J, Jakubek M, Platkevic M, Soukup P, Turecek D, Sykora V, et al. Large area pixel detector WIDEPIX with full area sensitivity composed of 100 timepix assemblies with edgeless sensors. J Instrum, JINST 2014;9:C04018. http://dx.doi.org/10.1088/1748-0221/9/04/C04018.
[13] Pichotka M. Iterative CBCT reconstruction-algorithms for a spectroscopic medipix-micro-CT. PhD thesis. University of Freiburg; 2014. https://www.freidok.uni-freiburg.de/data/9562.
[14] Pichotka M, Jakubek J, Vavrik D. Spectroscopic micro-tomography of metallic-organic composites by means of photon-counting detectors. J Instrum 2015;10:12.